Solar Physics (2023) 298:72
https://doi.org/10.1007/s11207-023-02159-w

RESEARCH

Kappa-Distributed Electrons in Solar Outflows: Beam-Plasma Instabilities and Radio Emissions

M. Lazar[1,2] · R.A. López[1,3] · S. Poedts[1,4] · S.M. Shaaban[5,6]

Received: 23 February 2023 / Accepted: 20 April 2023 / Published online: 29 May 2023

Abstract
Electrostatic (ES) wave instabilities are assumed to be at the origin of radio emissions from interplanetary shocks, and solar coronal sources are most likely induced by electron beams, more energetic but less dense than electron strahls in the solar wind. In this paper, we present the results of a new dispersion and stability analysis for electron populations with Kappa velocity distributions, as often indicated by in situ observations. We investigate, both theoretically and numerically, three electron plasma beam configurations with different implications in the generation of radio emissions. The same three cases, but for Maxwellian distributed electrons, were considered in numerical simulations by Thurgood and Tsiklauri (Astronomy and Astrophysics 584:A83, 2015). Our kinetic plasma approach clarifies the nature of the unstable mode as being an electron beam ES instability (and not a Langmuir instability) in all cases, and for both Kappa and Maxwellian approaches. Electron beam waves are Landau resonant and with frequencies of the fastest growing modes close to but below the plasma frequency (i.e., $\omega \lesssim \omega_{pe}$). Suprathermal Kappa tails tend to inhibit the instability by reducing the growth rates, but these effects become minor if the drift speed of the beam is sufficiently high compared to the thermal speed of the electrons. The frequency downshift, also revealed by the observations, clearly tends to increase in the presence of a Kappa-distributed beam. Particle-in-cell (PIC) simulations confirm the inhibiting effects of (initially) Kappa-distributed electrons, but these minor effects in the linear and quasi-linear phases unexpectedly lead to significant decreases in the wave energy levels of the (primary) ES fluctuations near the plasma frequency and higher harmonics. As a result, EM radio (secondary) emissions generated nonlinearly after saturation are even more drastically reduced and can even be completely suppressed. However, the EM emissions around the second harmonic ($\omega \lesssim 2\,\omega_{pe}$) are markedly powered by two symmetric countermoving beams, even in the presence of Kappa electrons. These results offer real promise for a realistic interpretation and modeling of radio emissions observed in heliosphere, arguing in favor of a rigorous spectral analysis of the wave instabilities at their origin.

1. Introduction

Radio electromagnetic (EM) emissions are true messengers that offer us information about the nature of their sources in the heliosphere (Pick and Vilmer, 2008; Reid and Ratcliffe, 2014), or in other stellar systems in our Galaxy (Crosley et al., 2016; Villadsen and Hallinan,

Extended author information available on the last page of the article

2019). The most accessible are the radio emissions generated by the activity of the Sun, such as type-III radio bursts from solar coronal flares preceding coronal mass ejections (CMEs) and type-II radio bursts (with herringbone-shapes in frequency-time diagrams) from the upstream regions of interplanetary shocks triggered by the CMEs (Pick and Vilmer, 2008; Reid and Ratcliffe, 2014; Jebaraj et al., 2021). Their decoding is facilitated by both remote and in situ observations by the ground-based interferometers and space-borne receivers (Pulupa, Bale, and Kasper, 2010; Thejappa, MacDowall, and Bergamo, 2012; Mann et al., 2018; Thejappa, 2022) and may provide the prerequisites for understanding those radio emissions whose distant sources are less accessible to direct measurements (Crosley et al., 2016; Villadsen and Hallinan, 2019).

Despite several decades of investigations, the origin of radio emissions observed from interplanetary shocks and flares in the solar corona still puzzles the space plasma community (Ratcliffe et al., 2014; Ziebell et al., 2016; Morosan et al., 2019; Lee et al., 2022). There is observational evidence that the accelerated electron beams must be the source of radio emissions (Gurnett, 1985; Mann et al., 2018; Soucek, Píša, and Santolík, 2019), but it is not yet clear what physical mechanisms are responsible for converting the kinetic energy of the electrons into EM radiation. The most invoked are the electrostatic (ES) instabilities of electron beams, especially Langmuir waves, also known as electron plasma waves (Ganse et al., 2012; Ratcliffe et al., 2014; Thurgood and Tsiklauri, 2015; Henri et al., 2019), which should reach sufficiently large amplitudes to decay nonlinearly and produce secondary EM waves (Reid and Ratcliffe, 2014; Henri et al., 2019). The presence of energetic beams is proven by in-situ measurements of electron velocity distributions in association with Langmuir ES fluctuations near the plasma frequency ω_{pe} or harmonics, e.g., $\sim 2\omega_{pe}$ (Pulupa, Bale, and Kasper, 2010; Mann et al., 2018; Soucek, Píša, and Santolík, 2019). Moreover, there are observational reports claiming that wave packets of Langmuir waves and ion-acoustic waves from the CME foreshocks and coronal flares may satisfy the conditions of resonant nonlinear interaction and generation of type-II and type-III radio bursts (Thejappa, MacDowall, and Bergamo, 2012; Thejappa, 2022).

ES instability requires the electron beam to be sufficiently energetic, that is, with the beam speed being higher than the thermal speed (talking about hot plasmas with temperatures above $10^5 - 10^6$ K), and the modes that develop the fastest, i.e., with the highest growth rate, are those that propagate parallel to the magnetic field (Cairns, 1989; Gary, 1993; López et al., 2020; Verscharen et al., 2022). The resulting enhanced fluctuations may contribute to the relaxation and thermalization of electron beams (Thurgood and Tsiklauri, 2015; Henri et al., 2019; Lee et al., 2019), possibly linking to suprathermal halo and strahl electron populations from the solar wind (Shaaban et al., 2018a, 2019; López et al., 2020; Micera et al., 2020), which have lower beam (or drift) velocities, but are responsible for the main heat flux (Wilson et al., 2019a,b). In this case, EM and hybrid waves are destabilized, known as heat-flux instabilities, e.g. whistler and firehose heat-flux instabilities (similar to those driven by the temperature anisotropy), with propagation parallel or oblique to the magnetic field (Shaaban, Lazar, and Poedts, 2018b; López et al., 2020; Micera et al., 2020; Lazar et al., 2023).

The nature of the unstable waves appears to be strongly conditioned by the properties of the interacting electron populations. Thus, in space plasmas the main high-density population is the electron core, to which a hotter but more diluted halo can be attached. In addition, up to a few keV, the observed velocity distributions often reveal a field-aligned, anti-sunward directed electron strahl/beam, more prominent at low heliospheric distances and in the high-speed winds (Maksimovic et al., 2005; Wilson et al., 2019a). Double strahls or counterbeaming electrons (also known as bi-directional electrons) are also observed in

the upstream regions of interplanetary shocks (due to the shock reflection and acceleration processes) and a closed magnetic field topology in, e.g., coronal loops and CMEs (Lazar et al., 2014; Cremades et al., 2015). In-situ observations have identified counterbeaming (or bidirectional) electrons in the plasma sources of type-II emissions (Bale et al., 1999; Cremades et al., 2015). In the source regions of solar type-III radio bursts electrons exhibit bump-on-tail distributions, i.e., beams with very low density, e.g., $<10^{-3}$ cm^{-3}, but very high speeds, e.g., $>0.2c$, where c is the speed of light in vacuum (Lin et al., 1981, 1986).

The configurations and properties of electron beams can vary significantly, and we can expect ES waves of different kinds, e.g., Langmuir, electron beam, or electron acoustic modes (Gary, 1993; López et al., 2020), which are observed in the upstream regions of interplanetary shocks (Lacombe et al., 1985; Fuselier, Gurnett, and Fitzenreiter, 1985; Onsager and Holzworth, 1990; Pulupa and Bale, 2008). Nevertheless, the mechanisms that destabilize these wave modes (e.g., resonant or non-resonant) also depend on the properties of the electron beam–plasma system (Gary, 1985; Cairns, 1989; Gary, 1993; López et al., 2020).

We investigate three electron beam–plasma configurations, here defined as cases 1, 2 and 3 (see Table 1), with various implications in the generation of radio emissions. Thurgood and Tsiklauri (2015) reported results from particle-in-cell (PIC) simulations for exactly these three cases, describing electron populations with drifting Maxwellian velocity distributions. Many other similar (or even identical) configurations have also been analyzed in PIC simulations or using the generalized theory of weak turbulence (WT), see discussions below (Baumgärtel, 2014; Ziebell et al., 2016; Henri et al., 2019; Lee et al., 2019). Our present analysis proposes a new and more general approach, modeling electron populations with Kappa, or κ-power law velocity distributions. In-situ observations from various heliocentric distances regularly prove the existence of Kappa-distributed electrons, which are almost Maxwellian at low energies (up to a few tens of eV), but decrease as a κ-power law at higher energies (Vasyliunas, 1968; Maksimovic et al., 2005; Stverak et al., 2008; Wilson et al., 2019a,b). The high-energy tails are enhanced by the suprathermal halo component, which can be distinguished from the core (Maksimovic et al., 2005; Stverak et al., 2008), but generally has a much smaller relative drift than the beam (Wilson et al., 2019a,b). If present, highly anisotropic electron beams are reproduced by Kappa distributions, not only across interplanetary shocks caused by CMEs (Wilson et al., 2019a,b), but also inside their magnetic clouds (Nieves-Chinchilla and Viñas, 2008). These data suggest that electron beams from plasma sources of radio emission, such as CME-driven foreshocks might as well have Kappa distributions. Such non-thermal models are supported by the profiles of the velocity distributions showing Kappa-like suprathermal tails in plasma sources of type-II emissions (Pulupa and Bale, 2008), and in source regions of solar type-III radio bursts (Lin et al., 1981; Lin, 1997). The presence of suprathermal populations in the solar corona is key to the velocity filtration model and an implicit heating of the corona (Scudder, 1992), but also to the formation of fast solar wind streams in the exospheric model (Pierrard and Lemaire, 1996). The enhanced suprathermal tails of Kappa distributions correspond to low values of κ exponent, while in the limit of a large $\kappa \to \infty$ these tails reduce, recovering the Maxwellian low-energy core (Lazar, Poedts, and Fichtner, 2015; Lazar, Fichtner, and Yoon, 2016). Therefore, the effect of suprathermal (less thermalized) populations from the high-energy tails can be highlighted by a direct comparison of the results obtained for Kappa distributions and those obtained for Maxwellian limits, e.g., for $\kappa \to \infty$ (Lazar, Poedts, and Fichtner, 2015; Lazar and Fichtner, 2021b).

In cases 1 and 2 we deal with two, markedly asymmetric populations of electrons, a highly dense core (subscript c) and a more dilute beam (subscript b), with counter-drifts or counterbeaming velocities ($U_{c,b}$) satisfying the zero density current condition

($n_c U_c + n_b U_b = 0$). Case 3 assumes three electron populations, the core and two symmetric counterbeams, also satisfying the zero density current condition. The unstable ES waves identified by Thurgood and Tsiklauri (2015) were Langmuir waves in case 1, and electron beam modes in cases 2 and 3. Regarding the nature of ES fluctuations in numerical simulations, their characterization is usually based on comparison with theoretical spectra of frequency dispersion as a function of wavenumber. By contrast to previous works that compare the simulation spectra with approximations of the ES dispersion relations, e.g., for Langmuir waves (Kasaba, Matsumoto, and Omura, 2001; Thurgood and Tsiklauri, 2015), here we will show that exact numerical solutions, rigorously derived from kinetic (linear) dispersion theory, can in certain cases lead to different conclusions on the nature of unstable waves. The forward propagating ES beam mode identified in case 2 was found slightly below the plasma frequency, at about 0.9 ω_{pe} (Thurgood and Tsiklauri, 2015), which can explain the frequency downshift reported by the observations (Onsager and Holzworth, 1990; Soucek, Píša, and Santolík, 2019).[1] A beam–plasma interaction with beam velocities on the order of the electron thermal velocity was suggested as an explanation for plasma oscillations above and below the plasma frequency (Fuselier, Gurnett, and Fitzenreiter, 1985). More recent observations associated wave frequencies below plasma frequency with the slow beams, with a beam speed to thermal speed ratio satisfying $U_b/\theta_e < 2.5$ (Soucek, Píša, and Santolík, 2019).

In the same PIC simulations, the saturation of the initial ES instability was associated with the relaxation of the electron beams, which merge to the bulk or core component, and form a characteristic plateau (Thurgood and Tsiklauri, 2015). Nonlinear radio emissions were obtained only for cases 1 and 3, both at the fundamental and second harmonic in case 1, and in case 3 only the second harmonic emissions. One hypothesis for the lack of radio emissions in case 2 is the violation of frequency conservation in the three-wave resonant nonlinear interaction, mainly due to a lower frequency of the beam mode (Thurgood and Tsiklauri, 2015). Case 1 shows that, contrary to the previous suggestions of Ganse et al. (2012), the production of these radio emissions is not conditioned by the presence of two counterbeams of electrons. For similar cases, high-resolution 1D PIC simulations confirmed the proton dynamics response in nonlinear decay/scattering of high-frequency Langmuir-like ES wave with the generation of ion-acoustic waves (Baumgärtel, 2014).[2] Notice however, that an increased free energy of the two electron counterbeams in case 3, may be sources of the second harmonic emissions (Reid and Ratcliffe, 2014), in agreement with the simulations of Ganse et al. (2012). In WT theory the fundamental emission is not greatly affected by the presence of counterbeams, but the harmonic emission is also more effective when the two beams are present (Ziebell et al., 2016). For these cases, PIC simulations also indicate the generation of the higher-harmonic of ES nonlinear waves (Thurgood and Tsiklauri, 2015), invoked already to formulate a generalized WT theory and explain the quasi-power-law spectrum of ES waves (Yoon et al., 2003; Gaelzer et al., 2003; Yi, Yoon, and Ryu, 2007), but also the occasional observations of high-harmonic EM emissions (Rhee et al., 2009).

In Section 2 we introduce the theoretical (kinetic) formalism applied to the electron populations, when described by drifting Kappa distributions. In order to highlight the effects of

[1] Although wavelengths of plasma oscillations below the plasma frequency satisfy $k\lambda_{De} \simeq 1$, the Doppler shift due to the motion of the solar wind is not sufficient to produce the observed frequency shifts (Fuselier, Gurnett, and Fitzenreiter, 1985).

[2] For an important ion response in the nonlinear effects, 1D PIC simulations suggest a ratio of beam energy to thermal energy of core electrons not less than 1 (Baumgärtel, 2014).

suprathermal tails, these distributions and the corresponding results are compared with those obtained for idealized models, e.g., drifting Maxwellian (i.e., in the limit of $\kappa \to \infty$). For these plasma beam configurations we derive the dispersion equations of ES waves propagating parallel to the regular magnetic field. The dispersion relations are then solved numerically, using the general DIspersion Solver for Kappa plasmas (DIS-K) (López, Shaaban, and Lazar, 2021), to rigorously characterize the full spectra of relevant stable and unstable modes, their frequencies, and growth/damping rates, as functions of the wave-number. Section 3 presents the results obtained from PIC simulations for the same cases 1, 2 and 3 with parameters summarized in Table 1, and contrast again between Kappa and Maxwellian distributed electrons. The main results are discussed in the last section (Section 4), where we also draw the conclusions of our study, and potential implications in the future observational analysis.

2. Predictions from Linear Kinetic Theory

2.1. Kappa vs. Maxwellian Distribution Models

For a homogeneous plasma of electrons (subscript e) and protons (subscript p), we assume two distinct counter-streaming populations of electrons, i.e., the main or core component (subscript c) and the electron beam (subscript b, such that the electron velocity distribution reads

$$f_e\left(v_\parallel, v_\perp\right) = \frac{n_c}{n_e}\, f_c\left(v_\parallel, v_\perp\right) + \frac{n_b}{n_e}\, f_b\left(v_\parallel, v_\perp\right). \tag{1}$$

Relative densities n_j/n_e $(j = c, b)$ are defined with respect to n_e, the total electron number density, equal to the ion density $n_e = n_i$.

For the study of high-frequency ES waves and instabilities, a sufficiently general approach should consider suprathermal electrons described by the Kappa velocity distributions, whose presence increases, in general, with heliocentric distance (Maksimovic et al., 2005; Pierrard et al., 2016; Lazar et al., 2020). According to the solar wind observations at various heliocentric distances both the core and beam populations, can be assumed drifting-Kappa distributed (Maksimovic et al., 2005; Nieves-Chinchilla and Viñas, 2008; Wilson et al., 2019a,b; Scherer et al., 2022)

$$f_{c,b}\left(v_\parallel, v_\perp\right) = \frac{1}{\pi^{3/2}\theta_j^3} \frac{\Gamma\left(\kappa_{c,b}+1\right)}{\kappa_{c,b}^{3/2}\Gamma\left(\kappa_{c,b}-1/2\right)} \left[1 + \frac{\left(v_\parallel \pm U_{c,b}\right)^2}{\kappa_{c,b}\,\theta_{c,b}^2} + \frac{v_\perp^2}{\kappa_{c,b}\,\theta_{c,b}^2}\right]^{-\kappa_{c,b}-1}. \tag{2}$$

The lower κ parameter the harder the high-energy tails enhanced by the suprathermal populations (Pierrard and Lazar, 2010). For the parallel velocity component the "+" applies to U_c and "−" to U_b, such that counter-drifting (or counter-beaming) speeds have opposite signs, i.e., $U_c < 0$ and $U_b > 0$, and satisfy the zero net density current condition $n_c U_c + n_b U_b = 0$ in a frame fixed to ions. The idealized Maxwellian models, specific to populations near thermal equilibrium and in the absence of suprathermals, are just limit cases recovered for very large $\kappa \to \infty$

$$f_{c,b}(v_\parallel, v_\perp) = \frac{1}{\pi^{3/2}\theta_{c,b}^3} \exp\left\{-\frac{(v_\parallel \pm U_{c,b})^2}{\theta_{c,b}^2} - \frac{v_\perp^2}{\theta_{c,b}^2}\right\}. \tag{3}$$

Thermal velocities $\theta_{c,b} = (2k_B T_{c,b}/m_e)^{1/2}$ are related to the corresponding temperatures $T_{c,b}$ of Maxwellian distributed populations. If $\kappa > 3/2$ is finite, kinetic temperatures of Kappa distributed populations (as given by the second order moments) are higher than the corresponding Maxwellian

$$T^{\kappa}_{c,b} = \frac{2\kappa_{c,b}}{2\kappa_{c,b} - 3} \frac{m_e \theta^2_{c,b}}{2k_B} > T_{c,b} = \frac{m_e \theta^2_{c,b}}{2k_B}. \tag{4}$$

Therefore, we will be able to evaluate the effects of superthermal electrons from the Kappa distributed populations through a direct contrast with the results obtained for the Maxwellian populations (Lazar, Poedts, and Fichtner, 2015; Lazar, Fichtner, and Yoon, 2016; Lazar et al., 2022b). For additional explanations and extensive analyzes of other waves and instabilities see the recent textbook edited by Lazar and Fichtner (2021).

Since heavier ions, mostly protons (subscript p) do not react to the high-frequency ES fluctuations, their velocity distribution can be reduced to a non-drifting ($v_{0p} = 0$) Maxwellian

$$f_p(v_\parallel, v_\perp) = \frac{1}{\pi^{3/2}\theta_p^3} \exp\left\{ -\frac{v_\parallel^2 + v_\perp^2}{\theta_p^2} \right\}, \tag{5}$$

with thermal velocity $\theta_p = (2k_B T_p/m_p)^{1/2}$ related to their temperature T_p.

2.2. Dispersion Relations

When triggered by electron beams, the fastest growing ES modes propagate parallel to the uniform magnetic field ($k\hat{k} \parallel \hat{B}_0$); this is well known for Maxwellian populations, see the textbook of Gary (1993) and references therein, and here below we will demonstrate that it is also valid for Kappa-distributed populations using numerical simulations. For propagation parallel to the magnetic field, when the EM waves decouple from the ES fluctuations, the last are described by the following dispersion relation

$$1 + \frac{\omega^2_{pe}}{k} \int dv^3 \frac{\partial f_0/\partial v_\parallel}{\omega - k v_\parallel} = 0, \tag{6}$$

for a generic initial distribution $f_0(v_\parallel, v_\perp)$. For our plasma system, with Kappa distributed electrons, as given in Equations 1–2, and Maxwellian protons, the dispersion relation 6 becomes

$$1 - \sum_{j=c,b} \frac{\omega^2_{pj}}{k^2\theta_j^2} Z'_\kappa(\xi_j) - \frac{\omega^2_{pp}}{k^2\theta_p^2} Z'(\xi_p) = 0, \tag{7}$$

in terms of the modified plasma dispersion function specific to Kappa distributed populations (Lazar, Schlickeiser, and Shukla, 2008)

$$Z_\kappa(\xi^\kappa) = \frac{1}{\sqrt{\pi\kappa}} \frac{\Gamma(\kappa)}{\Gamma(\kappa - 1/2)} \int_{-\infty}^{+\infty} \frac{(1 + x^2/\kappa)^{-\kappa}}{x - \xi} dx, \quad \Im(\xi) > 0 \tag{8}$$

and its first derivative $Z'_\kappa(\xi)$, with different arguments corresponding to our three distinct plasma populations

$$\xi_p = \frac{\omega}{k\theta_p}, \quad \xi_c = \frac{\omega + kU_c}{k\theta_c}, \quad \xi_b = \frac{\omega - kU_b}{k\theta_b}. \tag{9}$$

Of interest are modes induced by the beam, i.e., those that propagate in the same direction ($\mathbf{k}\cdot\mathbf{U_b} = kU_b$, implying, $\mathbf{k}\cdot\mathbf{U_c} = -kU_c$). Proton contribution is described by the standard plasma dispersion function (Fried and Conte, 1961) $Z(\xi)$ and its first derivative $Z'(\xi)$ (see below).

In the absence of suprathermal electrons the dispersion relation for (drifting) Maxwellian plasma populations reads (Gary, 1993)

$$1 - \sum_{j=c,b,p} \frac{\omega_{pj}^2}{k^2\theta_j^2} Z'(\xi_j) = 0, \tag{10}$$

in terms of the plasma dispersion function

$$Z\left(\xi_j\right) = \frac{1}{\sqrt{\pi}} \int_{-\infty}^{+\infty} \frac{\exp(-x^2)}{x - \xi_j} dx, \quad \Im(\xi_j) > 0, \tag{11}$$

and its derivative $Z'(\xi) = -2[1 + \xi Z(\xi)]$,

In terms of normalized quantities, i.e., $\tilde{\omega} = \omega/\omega_{p,e}$, $\tilde{k} = k\theta_e/\omega_{p,e}$, $\tau = T_p/T_e$, $\mu = m_p/m_e = 1836$, $V_c = U_c/\theta_e$, $V_b = U_b/\theta_e$, $N_c = n_c/n_e$, $N_b = n_b/n_e$, and assuming $\theta_c = \theta_b = \theta_e$, as in Thurgood and Tsiklauri (2015), we can rewrite the dispersion relation (7) in the following explicit form

$$\tilde{k}^2 = N_c Z'_{\kappa_c}\left(\frac{\tilde{\omega}}{\tilde{k}} + V_c\right) + N_b Z'_{\kappa_b}\left(\frac{\tilde{\omega}}{\tilde{k}} - V_b\right) + \frac{1}{\tau} Z'\left(\sqrt{\frac{\mu}{\tau}}\frac{\tilde{\omega}}{\tilde{k}}\right). \tag{12}$$

Here $\omega_{pe} = (4\pi n_e e^2/m_e)^{1/2}$ is given by the total number density of electrons. Notice also that the electron populations are not necessarily described by the same parameter κ, and we can distinguish between κ_c and κ_b, which can be different. In the classical approach when all populations are Maxwellian the dispersion relation reduces to

$$\tilde{k}^2 = N_c Z'\left(\frac{\tilde{\omega}}{\tilde{k}} + V_c\right) + N_b Z'\left(\frac{\tilde{\omega}}{\tilde{k}} - V_b\right) + \frac{1}{\tau} Z'\left(\sqrt{\frac{\mu}{\tau}}\frac{\tilde{\omega}}{\tilde{k}}\right). \tag{13}$$

These dispersion relations apply to the plasma systems with only two electron counterbeaming electron populations, with highly asymmetric number densities and relative drifts, but with similar temperatures (Baumgärtel, 2014; Thurgood and Tsiklauri, 2015). Exact solutions of the dispersion equations can be determined using the numerical solver called DIS-K (DISpersion Solver for Kappa distributed plasmas), which is capable of solving the full spectrum of stable and unstable wave modes (López, Shaaban, and Lazar, 2021).

2.3. ES Instabilities. Cases 1 and 2

We first analyze cases 1 and 2 in Thurgood and Tsiklauri (2015), where the electron components are described by Maxwellian velocity distributions, with the same temperature $k_B T_e = 200$ eV $\simeq 2.32 \times 10^6$ K, and, implicitly, the same thermal velocity $\theta_c = \theta_b = \theta_e = (2k_B T_e/m_e)^{1/2} = 0.55 \times 10^4\sqrt{T_e(\mathrm{K})}$ m s^{-1} $= 0.84 \times 10^7$ m s^{-1}, see also Table 1. According to the same setup in Thurgood and Tsiklauri (2015), protons are assumed to have a slightly lower temperature $T_p = 0.73\, T_e \simeq 1.70 \times 10^6$ K, implying a temperature contrast $\tau = 0.73$ and a thermal velocity $\theta_p = (2k_B T_p/m_p)^{1/2} = 1.28 \times 10^2\sqrt{T_p(\mathrm{K})}$ m s^{-1} $= 1.67 \times 10^5$ m s^{-1}. In Case 1 the beam has a very low number density, $N_b = n_b/n_e = 0.0057$

Table 1 Parameters describing electron-proton plasmas with distinct electron configurations, core-beam in cases 1 and 2, and symmetric core-counterbeams (with the same temperatures, relative densities and relative drifts) in case 3.

Parameters\Cases	1 (core-beam)	2 (core-beam)	3 (core-counterbeams)
$T_e = T_c = T_b$ (10^6 K)	2.32	2.32	2.32
$\theta_e = \theta_c = \theta_b$ (10^6 m s^{-1})	8.4	8.4	8.4
$T_p = 0.73\, T_e$ (10^6 K)	1.70	1.70	1.70
$N_b = n_b/n_e$	0.0057	0.05	0.05
U_b/θ_e	16	8	8

but a high drift or beam speed, $V_b = U_b/\theta_e = 16$, while in case 2 the beam is denser $N_b = 0.05$ but less energetic, with $V_b = 8$.

These high beam speeds, e.g., $U_b \simeq 0.43\ c$ in case 1 and $U_b \simeq 0.22\ c$ in case 2, are relevant for the source regions of type-III radio bursts (Lin et al., 1981, 1986). In case 2 the density of the electron beam is much higher than the observations, but in case 1 it approaches the observed values. However, in the mentioned observations the source regions of type-III emissions are encountered near the Earth, while for coronal plasma sources we can expect higher density beams. Similar parameterizations have been used by Henri et al. (2019), claiming relevance for type-III radio bursts expected to be reported from lower heliospheric distances by new missions like Parker Solar Probe and Solar Orbiter. As for type-II emissions, such as those generated in CME-driven foreshocks, electron beam properties are estimated indirectly, using either the characteristics of these emissions (Graham and Cairns, 2015), or the properties of the upstream region of the bow shock (Soucek, Píša, and Santolík, 2019), which appear to be similar to the plasma sources of type-II bursts (Pulupa and Bale, 2008). Thus, the electron beam densities considered here are perfectly relevant for plasma sources of type-II emissions, while the beam speed in cases 2 and 3 is the upper limit reported for instance in the bow shock (Soucek, Píša, and Santolík, 2019), although higher beam speeds might be expected in foreshocks closer to the Sun, as well as those associated with high speed CMEs.

Thurgood and Tsiklauri (2015) compared their simulations spectra with analytical (approximated) solutions of ES waves, while here in Figures 1 and 2 we present the exact solutions derived numerically for cases 1 and 2, respectively. Upper panels display the dispersion of the wave frequency (ω/ω_{pe}, normalized by the plasma frequency) as a function of the wave-number ($\theta_e k/\omega_{pe}$, normalized by the inverse of the Debye length $\lambda_{De} = \theta/\omega_{pe}$). In the lower panels we make a clear distinction between the stable and unstable solutions showing the normalized imaginary frequency (γ/ω_{pe}) as a function of the same normalized wave-number ($\theta_e k/\omega_{pe}$). If $\gamma \leq 0$ the wave mode is stable and damped, and if $\gamma > 0$ we deal with an unstable mode leading to instability.

We analyze and distinguish between two types of solutions that have raised debates regarding their association with ES instabilities at the origin of radio emissions (Ganse et al., 2012; Baumgärtel, 2014; Thurgood and Tsiklauri, 2015; Soucek, Píša, and Santolík, 2019). At higher wave frequencies in the upper panels, i.e., $\omega > \omega_{pe}$, the Langmuir waves (orange lines) change their dispersion profile in the presence of the beam, leading to higher phase velocities ω/k, which grow faster than for a nondrifting plasma with increasing the wave-number k, asymptotically approaching the beam speed $U_b > \theta_e$. These Langmuir waves are stable and for large k become highly damped with $\gamma < 0$ (orange lines in the lower panels). Only the electron beam modes (blue lines) are destabilized, with an almost linear dispersion

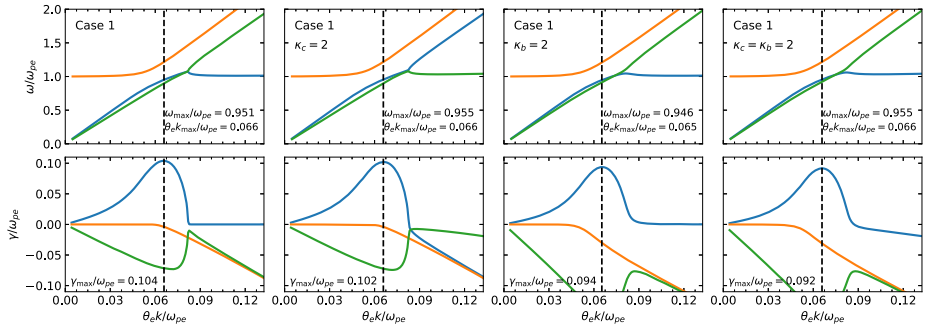

Figure 1 Wave frequency ω_r/ω_{pe} (upper panels) and growth/damping rates γ/ω_{pe} (lower panels) of Langmuir waves (orange) and electron-beaming modes (blue and green) for case 1 in Thurgood and Tsiklauri (2015) (left panels), compared with wave spectra modified by the presence of Kappa electrons in the core (second panels), the beam (third panels), or both the core and beam components (last panels).

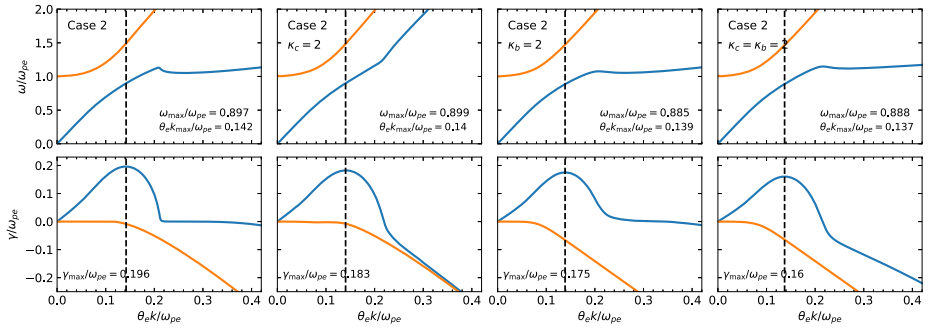

Figure 2 Wave frequency ω_r/ω_{pe} (upper panels) and growth/damping rates γ/ω_{pe} (lower panels) of Langmuir waves (orange) and electron-beaming mode corresponding to instability (blue) for case 2 in Thurgood and Tsiklauri (2015) (left panels) compared with wave spectra modified by the presence of Kappa electrons in the core (second panels), the beam (third panels), or both the core and beam components (last panels).

$\omega \simeq kU_b$ and growth rates ($\gamma > 0$) showing peaks of maximum values corresponding to the fastest growing modes. These unstable modes have frequencies close to but below the plasma frequency, causing them to often be confused with Langmuir waves, or identified as beam-modified Langmuir waves (Cairns, 1989; Omura et al., 1996). Moreover, such a frequency downshift is already confirmed by the observations in interplanetary foreshocks (Fuselier, Gurnett, and Fitzenreiter, 1985; Lobzin et al., 2005; Píša et al., 2016), and below we will show that it is enhanced in the presence of suprathermal Kappa tails of electron distributions.

First columns (left) display the exact solutions of the dispersion relation (13), when both electron populations are considered drifting Maxwellian ($\kappa \to \infty$), i.e., in the absence of suprathermal tails. As already mentioned, for both cases, we obtain an instability of beam modes (blue lines), whereas the Langmuir mode is stable (orange lines). Thurgood and Tsiklauri (2015) gave the same interpretation to the instability in case 2, but for case 1, they could not decouple and distinguish between these two modes and attributed the instability to Langmuir waves, most likely, because in case 1 the dispersion curves are closer to each other; for a comparison, see our Figures 1 and 2. The differences between the Langmuir and the electron beam modes are outlined primarily by the frequency dispersion as a function of

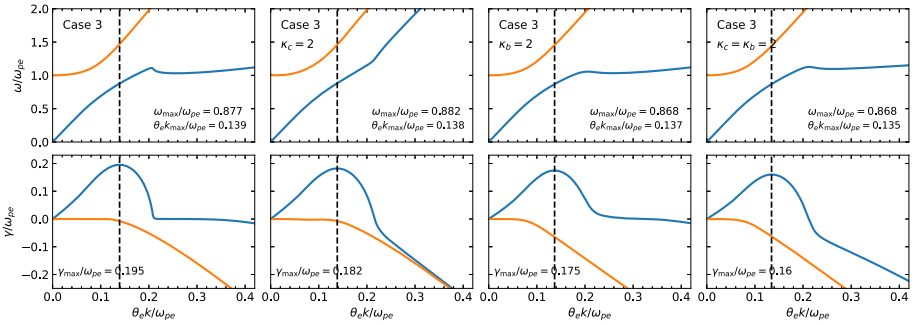

Figure 3 Wave frequency ω_r/ω_{pe} (upper panels) and growth/damping rates γ/ω_{pe} (lower panels) of Langmuir waves (orange) and electron-beaming mode corresponding to instability (blue) for case 3 in Thurgood and Tsiklauri (2015) (left panels), compared with wave spectra modified by the presence of Kappa electrons in the core (second panels), the beam (third panels), or both the core and beam components (last panels).

the wave number in Figures 1 – 3. Whereas Langmuir waves are limited to high frequencies, higher than the plasma frequency, the electron beam mode dispersion branch spans frequencies both below and above the plasma frequency (Cairns, 1989; Gary, 1993; Soucek, Píša, and Santolík, 2019). For cases like those analyzed here, at high wave numbers the (unstable) beam mode takes over the Langmuir dispersion and vice versa (Gary, 1993), and if the instability is excited close to the plasma frequency ω_{pe}, then it becomes difficult, both observationally or experimentally, to resolve the two different modes (Gary, 1993; Thurgood and Tsiklauri, 2015). We could further distinguish between them using the characteristics of their specific regimes, e.g., increased bandwidths of the beam mode fluctuations well below ω_{pe}, or narrow bandwidths of the Langmuir waves near ω_{pe} (Fuselier, Gurnett, and Fitzenreiter, 1985; Onsager and Holzworth, 1990; Soucek, Píša, and Santolík, 2019). Moreover, the regime of Langmuir instabilities is confined to electron beams with very low number densities, $n_b/n_e \leqslant 10^{-3}$ (Cairns, 1989; Gary, 1993).

In the comparative analysis, we investigate the effects of Kappa-distributed electrons for three distinct situations. First, we assumed that only one of the electron components has suprathermal enhanced tails, and if that is the core and the beam remains a drifting Maxwellian, the results are shown by the panels in the second columns of Figures 1 and 2 for $\kappa_c = \kappa = 2$. For the other case where the beam is described by a drifting Kappa and the core by a drifting Maxwellian, the results are shown in the third columns for $\kappa_b = \kappa = 2$. The dispersion relation to be resolved in each of these two cases is similar to that in Equation 13, except that the term for Kappa population takes the corresponding form from Equation 12. Then we considered that both the core and beam components are Kappa distributed, and are described by the dispersion relation 12. The ES solutions obtained for $\kappa_c = \kappa_b = \kappa = 2$ are displayed in the last columns of these two figures.

The modified Langmuir waves (orange lines) remain stable and damped, and the dispersion of their wave frequency as a function of the wave number (upper panels) does not suffer major changes in the presence of suprathermal electrons. Only damping rates are affected (lower panels), but mainly by the suprathermal tails in the beam component. Thus, in the panels from the last two columns, the inflection point where damping rate starts to increase corresponds to lower wave numbers than in the other two columns. This means higher damping rates, as already shown for stable ES waves (Lazar et al., 2022a).

Of greater interest are the electron beam instabilities (blue lines), whose wave frequency shows an almost linear wave-number dispersion, which is only slightly affected by the

suprathermal electrons. Their growth rates are however diminished, progressively with increasing the presence of suprathermals in the core and beam components. For instance, the maximum growth rates obtained in case 1 in Figure 1 decrease from $\gamma_{\max}/\omega_{pe} = 0.104$ for Maxwellian components to 0.102 for $\kappa_c = 2$, 0.094 for $\kappa_b = 2$, and 0.092 for $\kappa_c = \kappa_b = 2$. A similar lowering of the growth rates is also observed in case 2, from $\gamma_{\max}/\omega_{pe} = 0.196$ for Maxwellian components to 0.183 for $\kappa_c = 2$, 0.175 for $\kappa_b = 2$, and 0.092 for $\kappa_c = \kappa_b = 2$. This inhibition of the instability is generally due to the high-energy tails, which reduce the effective anisotropy of the electron beam–plasma system. Instead, the range of unstable wave numbers does not change, nor does the wave number corresponding to the maximum growth rate, because these properties depend mainly on the drift speed (as can be inferred from comparison of Figures 1 and 2).

Responsible for the instability are the beam electrons, which are Landau resonant with the ES beam waves ($\omega \simeq kU_b$), those with maximum growth rates satisfying $|\xi_{b,\max}| = |(\omega_{\max}/k_{\max} - U_b)/\theta_e| \gtrsim 1$, e.g., $|\xi_{b,\max}| \in [1.46, 1.59]$ for case 1 and $|\xi_{b,\max}| \in [1.52, 1.68]$ for case 2. The velocity distribution of beam population exhibits a positive slope, which gives not only the sign but also the magnitude of the growth rate, $\gamma \propto \partial f_b/\partial v_\parallel > 0$ (Gary, 1993). This slope is reduced in the presence of suprathermal tails, which explains the decrease of growth rates in Figures 1 and 2. The maximum growth rates are higher in case 2 because the beam is denser, involving more electrons in the resonant interaction, and the positive slope is implicitly higher. If the electron core is hotter due to the presence of suprathermals (2nd and 4th columns in Figures 1 and 2), then the growth rates drop to zero and become quickly negative with increasing wave-number, i.e., the beam mode becomes damped in this case. This corresponds to the one of the two complex conjugate solutions of the beam mode, one responsible for instability and the other one damped; for a detail in Figure 1, see the blue and green lines, respectively. For the regimes of a cooler beam, e.g., when $T_b < T_c$, the dispersion curves of the wave frequencies and growth rates of these two beam modes cross each other, but they may also markedly decouple for hotter beams with $T_b > T_c$ (Cairns, 1989), e.g., in the last two columns of Figure 1, due to the beams with suprathermal tails.

The decreases in growth rate obtained for Kappa distributions are however small. This is because in both cases the drift or beam speed is higher or even much higher than the thermal spread, and the influence of the suprathermal tails remains low. The electrons with enhanced Kappa tails are hotter than those with Maxwellian distributions, i.e., for $\kappa = 2$, from Equation 4 we find $T_\kappa = 4\ T_e = 800$ eV $\simeq 9.28 \times 10^6$ K, implying a higher thermal spread $\theta_\kappa = 0.55 \times 10^4 \sqrt{T_\kappa(\mathrm{K})}$ m/s $= 1.68 \times 10^7$ m/s $= 2\theta_e$, but which is still lower or much lower than the beam speed, $U_b = 16\,\theta_e$ in case 1 and $U_b = 8\,\theta_e$ in case 2. We can expect major effects of the suprathermal tails when the drift/beam speed is lower and near the threshold value, e.g., only a few times higher than the thermal speed. In such a case the effective anisotropy of the electron beam can be significantly reduced, for instance, by the formation of a plateau in the distribution, between the electron beam and the core population (Lazar and Fichtner, 2021b). Suprathermal tails can thus cause a switch from the regime of ES instabilities to a different one specific to EM or hybrid instabilities (López et al., 2020).

2.4. ES Instabilities. Case 3

The plasma system becomes more complex in case 3 by assuming three electron components: two symmetric counterbeams, basically with the same properties as the beam in case 2 (see Table 1) plus the core population, this time a nondrifting core (with respect to protons) with $V_c = 0$, and slightly lower density $N_c = 0.9$. If we describe the electron populations

with generalized drifting-Kappa distributions, then the dispersion relation for parallel ES waves becomes

$$\tilde{k}^2 = N_c Z'_{\kappa_c}\left(\frac{\tilde{\omega}}{\tilde{k}}\right) + N_1 Z'_{\kappa_1}\left(\frac{\tilde{\omega}}{\tilde{k}} - V_1\right) + N_2 Z'_{\kappa_2}\left(\frac{\tilde{\omega}}{\tilde{k}} + V_2\right) + \frac{1}{\tau} Z'\left(\sqrt{\frac{\mu}{\tau}}\frac{\tilde{\omega}}{\tilde{k}}\right), \qquad (14)$$

where the terms related to electron counterbeams are identified by subscripts 1 and 2. To outline the effects of Kappa-distributed electrons, we will compare solutions of Equation 14 with those of a classical approach, when all populations are Maxwellian, and this dispersion relation reduces to

$$\tilde{k}^2 = N_c Z'_j\left(\frac{\tilde{\omega}}{\tilde{k}}\right) + N_1 Z'\left(\frac{\tilde{\omega}}{\tilde{k}} - V_1\right) + N_2 Z'\left(\frac{\tilde{\omega}}{\tilde{k}} + V_2\right) + \frac{1}{\tau} Z'\left(\sqrt{\frac{\mu}{\tau}}\frac{\tilde{\omega}}{\tilde{k}}\right). \qquad (15)$$

The ES wave solutions are displayed in Figure 3, following the sequence as in Figures 1 and 2, the first column showing solutions of Equation 15 for Maxwellian populations, and the last column solutions of Equation 14, when both electron populations are Kappa distributed with $\kappa_c = \kappa_b = \kappa = 2$. In the second column, we have the ES spectra obtained when only the electron core has suprathermal tails with $\kappa_c = 2$, and in the third column when only the beam is Kappa-distributed with $\kappa_b = 2$. The dispersion relation to be resolved in each of these two cases is similar to that in Equation 15, except that the term for Kappa population takes the corresponding form from Equation 14. The wave spectra do not change visibly from those in Figure 2, Langmuir waves (orange lines) remain stable and damped, and the instability is predicted only for beam modes (blue line). However, in this case, we deal with two unstable beam modes in both directions of propagation along the magnetic field corresponding to positive and negative k. Because of symmetry, we omit backward solutions and show only forward propagating modes with positive $k > 0$. The frequency corresponding to the maximum growth rate is again not much departed from plasma frequency, but is slightly lower than case 2 and has the same tendency to decrease if the electron beam is Kappa distributed (last two columns). Despite the differences in the new configuration with symmetric electron counterbeams and a lower relative density of the core, the growth rates remain mainly depending on the beam properties so that their wave-number dispersion is not affected, and maximum growth rates reach the same values as the corresponding ones in case 2.

When the frequency downshift is more pronounced, as in cases 2 and 3 (for lower drift velocities), it tends also to increase in the presence of beams with Kappa tails. This frequency downshift may prevent the resonant nonlinear decay and subsequent generation of fundamental EM emission; but in case 3 the frequency mismatch can be compensated by the counterpropagating beam modes, which are able to couple nonlinearly and generate radio emissions of second harmonic (Thurgood and Tsiklauri, 2015). In the next section, we analyze these emissions using the results from PIC simulations with a particular emphasis on the effects introduced by the Kappa-distributed electrons.

3. PIC Simulations

We study the time evolution of the wave instability and their nonlinear decay leading to EM emissions using a 2D explicit PIC code based on the KEMPO1 code from Matsumoto and Omura (1993). Our simulation domain is 1024×1024 grid cells, with $L_x = L_y = 46.08\, c/\omega_{pe}$ and 625 particles per grid per species. The ratio of plasma frequency to electron

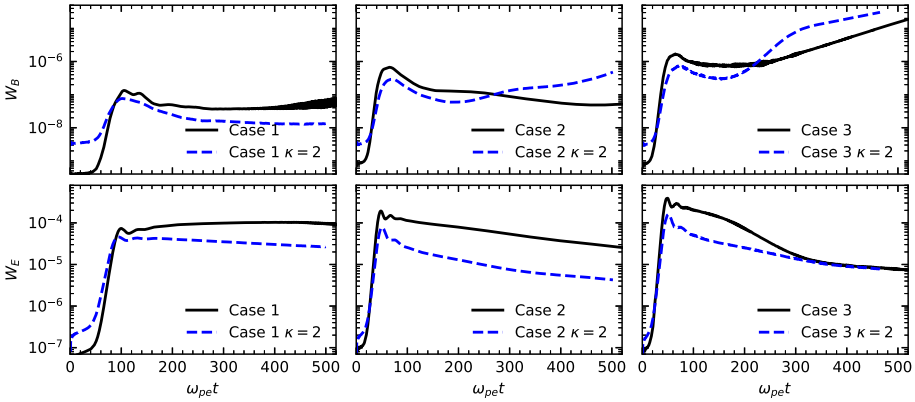

Figure 4 Temporal evolution of the total magnetic (upper) and electric (lower) wave energy densities (normalized), W_B and W_E, respectively, for cases 1 (left), 2 (middle), and 3 (right). See text for additional details.

gyro-frequency is $\omega_{pe}/\Omega_{ce} = 100$, and for the proton-to-electron mass ratio, we considered the real value $m_p/m_e = 1836$. The simulation lasts until $t_{\max} = 500/\omega_{pe}$ with a time step $\Delta t = 0.01/\omega_{pe}$. Note that here we adopt a realistic setup as for a space plasma embedded in the interplanetary magnetic field, by contrast to previous simulations, which considered unmagnetized plasma systems (Baumgärtel, 2014; Thurgood and Tsiklauri, 2015).

Figure 4 displays the total magnetic (upper panels) and electric (lower panels) wave energy densities normalized by the energy density of the interplanetary (uniform) magnetic field. These are computed by integration in the simulation domain of wave energy densities (normalized), namely as $W_B = \int dxdy\ \delta B^2/B_0^2$ and $W_E = \int dxdy\ \delta E^2/B_0^2$, respectively. We present the results for all three cases but compare the wave energy densities only for the extreme situations, namely, when both populations are Maxwellian distributed (black lines) with that when both are described by Kappa distributions (blue dashed lines). Linear theory suggests a similar (if not less) contrast for intermediate situations where only one of the electron populations has a Kappa distribution (see the wave spectra in the 2nd and 3rd columns in Figures 1–3).

In Figure 4 the wave power reached at the instability saturation is clearly dominated by W_E of ES fluctuations, which is more than two orders of magnitude higher than W_B. The peaks reached by W_E and W_B in the quasi-linear growth depend on the nature of the initial distributions, as do their temporal profiles after saturation. These peak values of the electric and magnetic wave power are higher in case 2 than in case 1, and higher in case 3 than in 2, because the initial kinetic energy of the electron beam (i.e., the free-energy source of the instability) increases in the same way. In full agreement with the linear theory, the growth slopes (roughly proportional to the growth rates) and the peak values of W_E and W_B are lower when the electrons are Kappa distributed (blue dashed lines), compared to the Maxwellian case (black lines). This difference remains so with increasing time in case 1, and also in case 2, but only for W_E, whereas the temporal variations of wave magnetic power W_B contrast markedly. Thus, after a slow decrease, W_B for Kappa-distributed electrons (blue dashed line) shows a turning point and starts increasing around $\omega_{pe}t = 180$. This enhancement of EM wave energy due to suprathermal tails increases and persists toward the end of the simulation runs, e.g., in the time interval $\omega_{pe}t = [400-500]$.

In case 3, apparently due to the presence of two counterbeaming electrons, an increase of W_B on long run is specific to both simulations. It is however faster for the electrons with

(initial) Kappa distributions, but the difference from the Maxwellian case is reduced toward the end of simulations. W_E shows a systematic decrease, and this difference cancels out completely, and much faster, already at $\omega_{pe}t \simeq 300$. In this case after saturation, nonlinear wave–wave mixing seems to contribute to a substantial conversion of energy from ES to EM fields, and the values reached by W_B may exceed those of W_E. The same conclusion can be drawn in case 2 but, somewhat surprisingly, only for the simulation with Kappa-distributed electrons. We will explain these differences in the next section through a more detailed spectral analysis.

3.1. From ES Instabilities to Radio Emissions

Now let us look at the details of the enhanced fluctuations resulting from instabilities, including daughter waves such as the radio EM emissions reported in observations, in the vicinity of the plasma frequency or its harmonics. In Figures 5, 7, and 9, we plot the space–time FFTs of the spectral (normalized) wave energy density (color coded in the bars on the right) computed for the parallel component of the electric field, $|\mathrm{FFT}(\delta E_\parallel/B_0)|^2$, in cases 1, 2, and 3, respectively, as a function of the (normalized) wave frequency and wave number. Figures 6, 8, and 10 show the corresponding FFTs of the (normalized) magnetic energy density computed for the perpendicular magnetic field, namely, the out-of-plane ($B_\perp \simeq B_z$) component $|\mathrm{FFT}(\delta B_\perp/B_0)|^2$. These plots again compare the results obtained for an idealized Maxwellian approach (upper panels) with the new ones for electron populations described by Kappa distributions (lower panels). Corresponding to the three columns, the energy density integrated over three time intervals are presented, respectively, $50 < \omega_{pe}t < 150$, $400 < \omega_{pe}t < 500$, and the entire running period $0 < \omega_{pe}t < 500$. In the first interval immediately after saturation, i.e., $50 < \omega_{pe}t < 150$, the temporal profiles obtained for W_E and W_B in Figure 4 show similar contrasts, i.e., the fluctuating energy decreases in the presence of Kappa-distributed electrons. Besides, the second interval, i.e., $400 < \omega_{pe}t < 500$, is more relevant for the EM radio emissions resulted from the nonlinear decay of the enhanced ES fluctuations. In this range (see Figure 4) the influence of the (initial) Kappa tails on W_E and W_B does not remain the same and also varies from case to case.

In case 1 the counterdrifting Maxwellian electrons (upper panels) are very prolific, producing intense and rich spectra with wave energy density maxima of the fundamental excitation close to but below the plasma frequency ($\lesssim \omega_{pe}$), and maxima of the second ($\lesssim 2\omega_{pe}$) and third harmonics ($\lesssim 3\omega_{pe}$), which are visible for ES fluctuations in Figure 5. The EM radio spectra show an obvious symmetry in Figure 6, with maxima of fundamental (around ω_{pe}) and higher harmonics (around $2\omega_{pe}$ and $3\omega_{pe}$) in both forward ($k > 0$) and backward ($k < 0$) directions of propagation. Early in time, only the growing fluctuations of the electron beam instability (dashed red lines) reach significant energy density levels, whereas the Langmuir wave fluctuations (dashed white lines) remain at the noise level. The guiding lines, dashed red and dashed white, reproduce the dispersion relations for, respectively, the beam and Langmuir modes, from Figure 1. The maximum (peak) levels of energy density correspond to the frequency ($\omega_{\max}$) and wave-number ($k_{\max}$) of the fastest growing beam modes, i.e., with the maximum growth rates obtained in Figure 1. Despite a minor decrease of these growth rates (also minor variations of the corresponding wave frequency and wave number) caused by the (initial) Kappa tails, the wave energy density suffers a significant reduction after saturation; see lower panels in Figures 5 and 6. The dispersion profiles of the ES beam modes are still visible, and their maxima are sufficiently intense (Figure 5), whereas the EM emissions decrease significantly, keeping only dispersion profiles at quasi-thermal noise level, without any noticeable maximum. These results are in agreement with

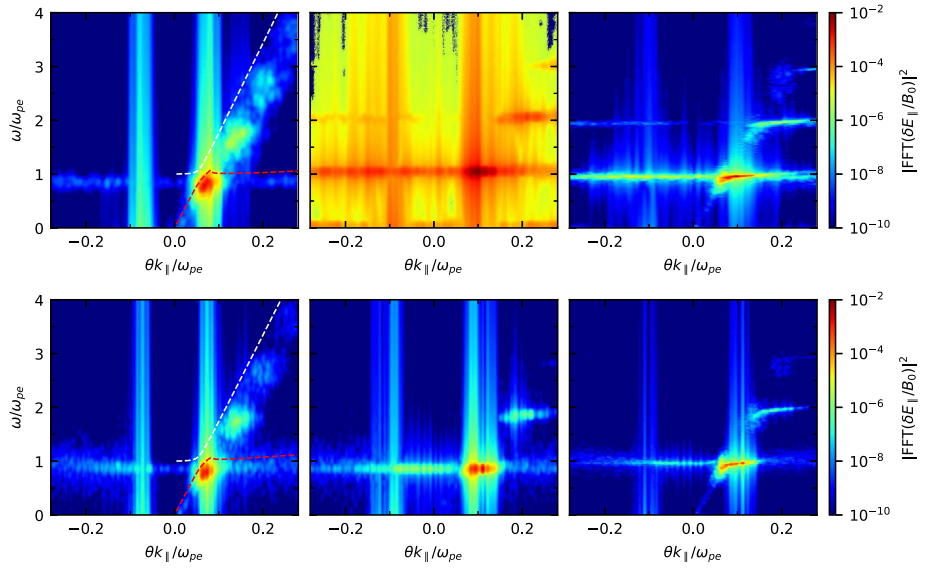

Figure 5 Space–time FFTs (at $k_\perp = 0$) of the $\delta E_x^2/B_0^2$ for the following time intervals (from left to right): $50 < \omega_{pe}t < 150$, $400 < \omega_{pe}t < 500$, and $0 < \omega_{pe}t < 500$ for case 1 with Maxwellian (upper) and Kappa electrons with $\kappa_c = \kappa_b = 2$ (lower).

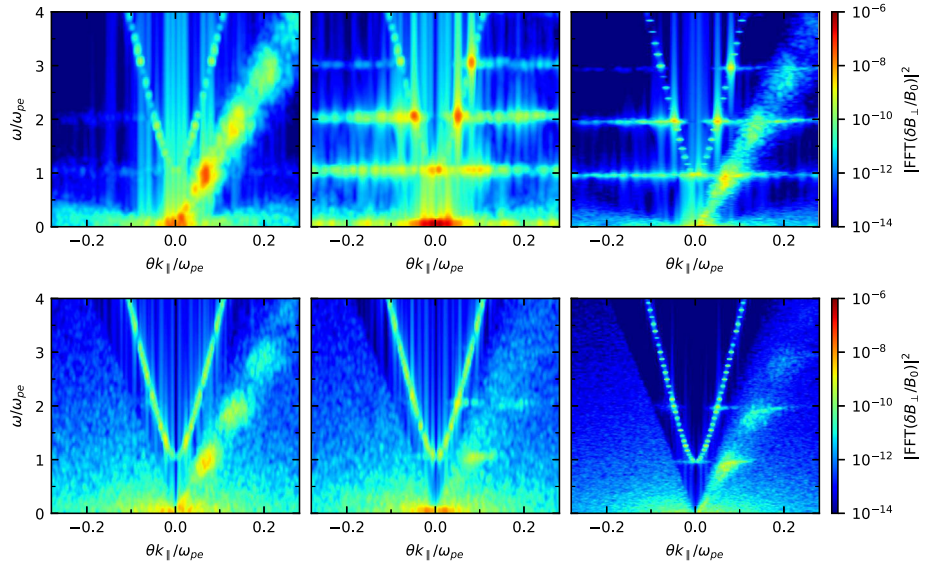

Figure 6 Space–time FFTs (at $k_\perp = 0$) of the $\delta B_z^2/B_0^2$ for the following time intervals (from left to right) $50 < \omega_{pe}t < 150$, $400 < \omega_{pe}t < 500$, and $0 < \omega_{pe}t < 500$, for case 1 with Maxwellian (upper) and Kappa electrons with $\kappa_c = \kappa_b = 2$ (lower).

the lower peaks reached after the quasi-linear growth (e.g., in Figure 4) but also suggest that nonlinear wave decay processes at the origin of radio emissions are very sensitive to the

Manley–Rowe laws of conservation for the wave energy (wave frequency) and momentum (wave number) (Manley and Rowe, 1956).

In general, Langmuir modes are considered more efficient than beam modes in producing radio emissions, because the latter tend not to satisfy the nonlinear resonant conversion (wave–wave interaction) with decreasing frequency and wave number. Our results identify for case 1 those beam modes that can produce radio emissions when their frequencies are sufficiently high and close to ω_{pe}. In the nonlinear conversion an important role can be played by the low-frequency (daughter) waves, e.g., the ion-acoustic waves, which are however not observed in Figure 5. Instead, Figure 6 shows low-frequency transverse waves, which may eventually couple with the ES beam modes to explain the generation of radio emissions at fundamental and higher harmonics. Future studies will have to clarify the nature of these low-frequency EM waves (see below the alternative explanations offered by Thurgood and Tsiklauri (2015) for the generation of 2nd-order harmonics in case 3).

For case 2, the spectra of ES fluctuations and EM emissions are displayed in Figures 7 and 8. Fluctuations of the beam modes remain significantly more intense (compared to the Langmuir modes), both at the fundamental frequency ($\lesssim \omega_{pe}$), with maximum intensity corresponding to the maximum growth rates, but also to the higher harmonics. The spectrum of EM emissions is much poorer than in case 1. For Maxwellian electrons (upper panels), only two and very narrow maxima of the second harmonic (around $2\omega_{pe}$) are obtained in the forward ($k > 0$) and backward ($k < 0$) directions of propagation. For the same electron configuration but in the absence of the background magnetic field, previous simulations by Thurgood and Tsiklauri (2015) did not identify these radio emissions. Kappa tails have the same inhibiting effect (lower panels), significantly reducing both ES fluctuations and EM emissions and making the peaks of the latter imperceptible.

In case 3, we expect the wave spectra to be very similar to case 2 but more symmetric. Indeed, the spectra of ES fluctuations and EM emissions in Figures 9 and 10 are symmetric, but the levels reached by the wave fluctuations are markedly different. Thus, if we compare to case 2, then the maximum (peaking) levels of ES fluctuations in Figure 9 are much lower than in Figure 7, whereas the EM radio emissions in Figure 10 have much higher intensities compared with Figure 8 in both forward ($k > 0$) and backward ($k < 0$) directions of propagation. The peaks are specific to the second harmonic emissions, whose intense spectra exhibit a remarkable spread (above and below 2 ω_{pe}) along the dispersion curves of free-EM modes. These results are also consistent with a general WT approach, applied, for instance, by Ziebell et al. (2016), who found that for Maxwellian electrons, the harmonic emission becomes more effective when the two counterbeams are present. In case 3 the energy of ES fluctuations decreases in intensity as compared to case 2 (see Figure 4), but it is much more efficiently converted into EM radio emissions. The two symmetric electron beams induce two counterpropagating ES waves, which may couple directly, without involving ion-acoustic waves, and generate daughter EM waves near the second harmonics in both forward and backward directions.

If we compare the EM emissions in Figure 10, then the energy density levels (including peak values) produced by Kappa-distributed electrons (lower panels) are lower but still comparable to those induced by Maxwellian electrons (upper panels). We remind that Figures 6, 8, and 10 display only the parallel propagating (i.e., k_x) component of radio emissions, which may have a more or less isotropic spectrum. For a comparison, the complete spectra of EM emissions as functions of both k_x and k_y are plotted in Figure 11 in the Appendix. The presence of Kappa high-energy tails in the initial distributions leads to total EM emissions with markedly enhanced intensities, explaining also the late increase of W_B in Figure 4. However, this increase seems to be mainly due to another highly anisotropic component of

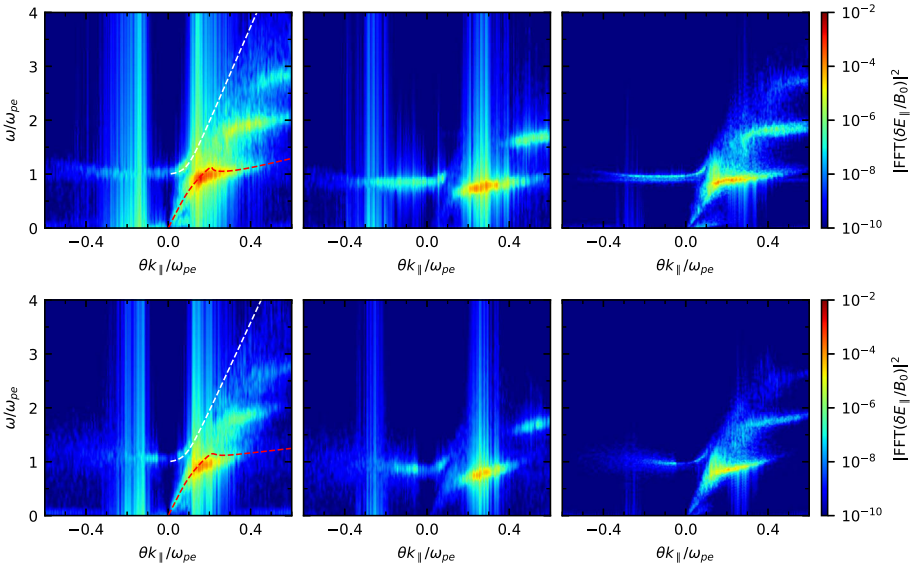

Figure 7 Space–time FFTs (at $k_\perp = 0$) of the $\delta E_x^2/B_0^2$ for the following time intervals (from left to right): $50 < \omega_{pe}t < 150$, $400 < \omega_{pe}t < 500$, and $0 < \omega_{pe}t < 500$ for case 2 with Maxwellian (upper) and Kappa electrons with $\kappa_c = \kappa_b = 2$ (lower).

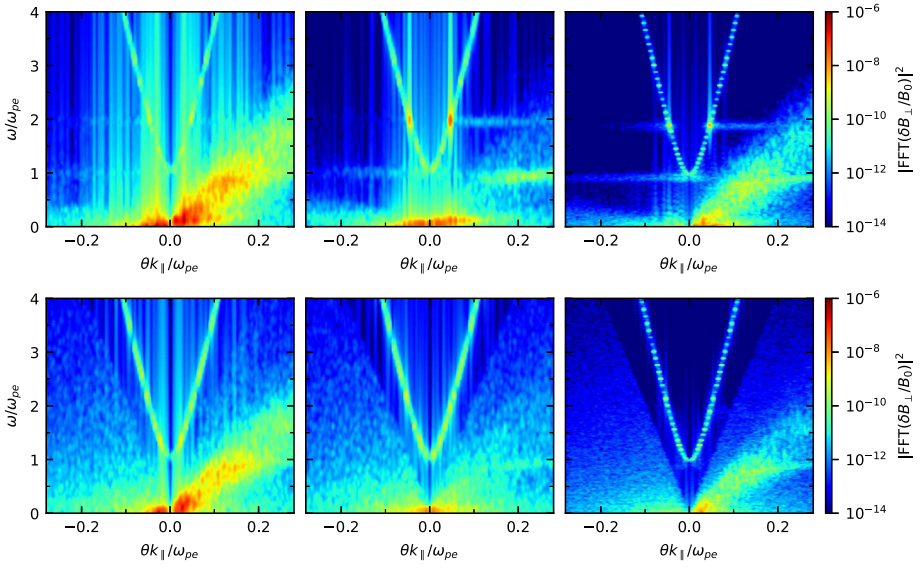

Figure 8 Space–time FFTs (at $k_\perp = 0$) of the $\delta B_z^2/B_0^2$ for the following time intervals (from left to right): $50 < \omega_{pe}t < 150$, $400 < \omega_{pe}t < 500$, and $0 < \omega_{pe}t < 500$ for case 2 with Maxwellian (upper) and Kappa electrons with $\kappa_c = \kappa_b = 2$ (lower).

fluctuating EM fields with perpendicular propagation (for $k_x = 0$), as explicitly shown in Figure 11. This excitation could be associated with the so-called filamentation instability of

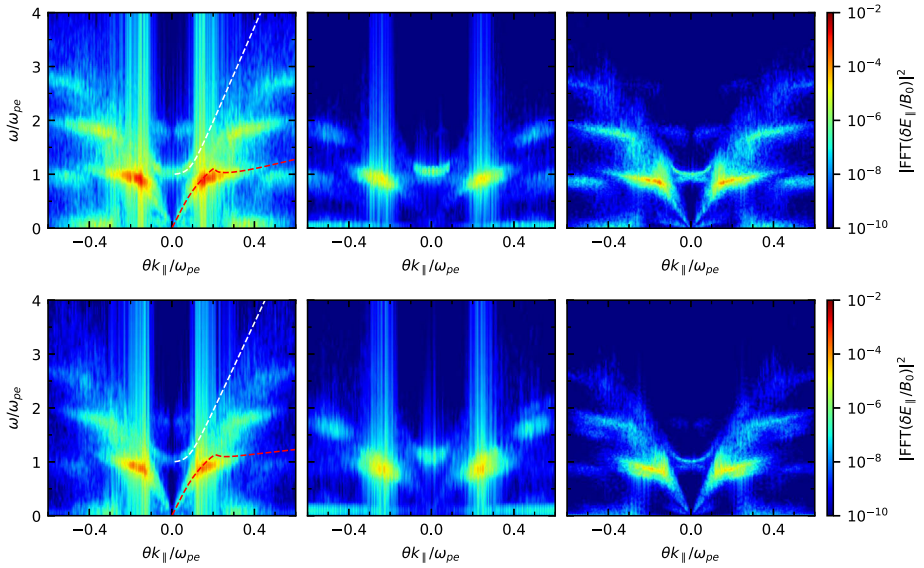

Figure 9 Space–time FFTs (at $k_\perp = 0$) of the $\delta E_x^2/B_0^2$ for the following time intervals (from left to right): $50 < \omega_{pe}t < 150$, $400 < \omega_{pe}t < 500$, and $0 < \omega_{pe}t < 500$ for case 3 with Maxwellian (upper) and Kappa electrons with $\kappa_c = \kappa_1 = \kappa_2 = 2$ (lower).

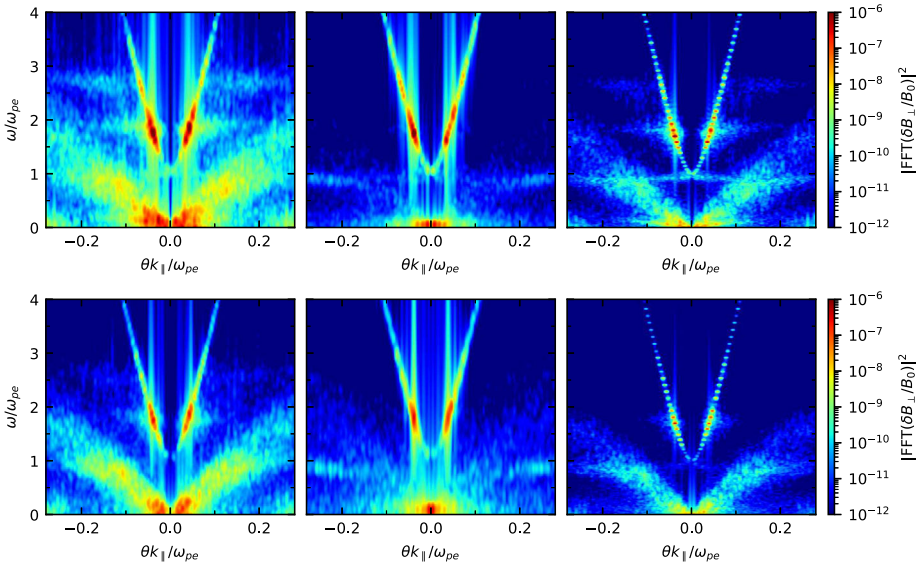

Figure 10 Space–time FFTs (at $k_\perp = 0$) of the $\delta B_z^2/B_0^2$ for the following time intervals (from left to right): $50 < \omega_{pe}t < 150$, $400 < \omega_{pe}t < 500$, and $0 < \omega_{pe}t < 500$ for case 3 with Maxwellian (upper) and Kappa electrons with $\kappa_c = \kappa_1 = \kappa_2 = 2$ (lower).

counterbeaming electrons (Fried, 1959), a Weibel-like instability (Weibel, 1959; Lazar et al., 2009), which can destabilize the ordinary mode. This instability has already been identified

in numerical simulations with similar setups (Lazar et al., 2023) or without a background magnetic field (Thurgood and Tsiklauri, 2015). Why this EM component is intensified in the nonlinear phase remains however a question to be answered by the future studies.

4. Conclusions

The EM radio emissions associated with energetic solar eruptions, as well as the interplanetary shocks caused by CMEs represent subjects of high interest in solar physics with potential applications in other stellar systems in our Galaxy. Understanding the properties and origin of radio emissions from interplanetary sources for which remote observations are complemented by in situ measurements allows us to develop realistic radiative models. Such reliable models are therefore crucial for decoding those emissions with less accessible sources, such as in the solar corona and other astrospheres. The most invoked are the ES wave instabilities of electron beams, which can convert their (free) energy into EM radio waves. Definitive answers regarding the involvement of these instabilities require not only a realistic parameterization, but also a kinetic modeling of the electron populations, e.g., the core and the beam, modeling their velocity distributions according to in situ observations.

In the present work, we investigated three electron plasma beam configurations, identified as cases 1, 2, and 3 (e.g., in Table 1), where electron core and beam populations were modeled with the drifting Kappa velocity distributions indicated by the in situ observations. Similar or even identical beam-plasma configurations have been previously examined in numerical simulations, applying, however, idealized distribution models, i.e., drifting Maxwellian distributions (Baumgärtel, 2014; Thurgood and Tsiklauri, 2015). In Section 2, we accurately derived the (linear) spectrum of stable and unstable ES waves on the basis of a rigorous kinetic plasma approach. For each of the three cases, we compared the wave spectra obtained for idealized drifting-Maxwellian distributions with those obtained in three distinct situations, namely, when a drifting-Kappa model is associated only with the core, or only with the beam, or with both electron populations. The exact wave spectra, e.g., in Figures 1, 2, and 3, allowed us to precisely identify the nature of the unstable modes. In all our cases the electron beam modes are destabilized, even for case 1 with (drifting-)Maxwellian distributions, for which Thurgood and Tsiklauri (2015) estimated a different instability of Langmuir waves. In case 1 the dispersion curves of the electron beam and Langmuir modes are indeed very close to each other, especially in the frequency range of the instability, so that only an exact numerical solution of the wave spectra can distinguish between them and identify the unstable mode. Our results are also supported by the values of the parameter $P = (n_b/n_e)^{1/3}(U_b/\theta_b)$, generally greater than 1, which are usually specific to a beam mode instability.[3]

In all analyzed cases the beam instabilities are excited by Landau resonance with the electron beam population. Because the characteristic frequencies (corresponding to major growth rates) are still close to the plasma frequency, $\omega \lesssim \omega_{pe}$, we deal with the kinetic regimes of electron beam instability, excited by resonant (or weakly resonant) electrons in the beam. Another proof in support of this statement is given by the values of $P \in (1.4, 3.0)$, which are above unity but are not very high. Moreover, the beam speed is sufficiently high compared to the thermal speed of the electrons, and we can estimate these kinetic regimes as being near the separation boundary from the fluid regime of the electron beam instabilities.

[3]Refer to Cairns (1989), Gary (1993), and Thurgood and Tsiklauri (2015) for more details on the relevance of this parameter in delimiting the regimes of Langmuir and electron beam instabilities.

For the same reason, the effects of the suprathermal tails are not major, becoming noticeable only when present in the distribution of the electron beam. Kappa tails tend to inhibit the instability by decreasing the maximum growth rate. In all cases investigated here, the wave frequency corresponding to the fastest growing mode is slightly lower than ω_{pe}. This frequency downshift has been reported by the observations, and we found that it tends to increase if the beam is Kappa distributed.

The PIC simulations confirm the inhibiting effects of the (initially) Kappa-distributed electrons, but also show that the small differences obtained in the linear and quasi-linear phases actually lead to a significant reduction in the energy of ES fluctuations after saturation. This also affects the nonlinear decay/coupling of ES fluctuations and causes secondary EM emissions, interpreted as radio emissions, to be markedly reduced and even completely suppressed. We can thus conclude that the electron beam–plasma configurations investigated here remain susceptible to ES instabilities, namely electron beam instabilities, but for electrons with Kappa tails, not all of them keep the same relevance in the radiative processes of radio emissions. For instance, when both the core and beam populations are Kappa distributed, the results from simulations showed reasonable (peaking) levels of EM energy density only for the second harmonic emissions in case 3. In this case the EM nonlinear emissions appear to be powered by two symmetric electron beams, capable of inducing two counterpropagating ES waves, which can couple directly (without involving ion-acoustic waves) and generate daughter EM waves near the second harmonics.

Our results prove that beam modes can be efficient in producing radio emissions, especially when these modes are excited below but very close to plasma frequency (minor downshift). The fundamental radio emission is produced at the plasma frequency and not below and appears to result from the coupling of beam modes with low-frequency EM waves rather than iono-acoustic waves (which may not be supported by the low temperature contrast between electrons and protons). Beam modes were never reported from the source regions of type III or type II radio bursts, but the present results should motivate future observations to perform a refined analysis of the plasma sources, analogous to the identification of beam modes in the Earth's foreshock (Fuselier, Gurnett, and Fitzenreiter, 1985; Onsager and Holzworth, 1990).

The present analysis paves the way for a realistic and rigorous modeling of ES instabilities at the origin of radio emissions caused by solar events. Future studies should also consider conditions closer to the beam instability thresholds, but also the more restrained parametric regime of the instability of Langmuir modes (more or less modified by the presence of the beam), which requires the beam density to be even lower than those assumed here (i.e., $n_b \leqslant 10^{-3} n_e$). With the insights gained in our present analysis, we can anticipate that the presence of suprathermal Kappa tails in the electron beam–plasma distributions could significantly modify these thresholds or critical conditions of ES instabilities. We can also conclude that such parametric studies can benefit not only from numerical simulations, but also from a rigorous theoretical prescription of the spectra of unstable modes based on realistic modeling of electron velocity distributions.

Appendix: 2D Spectra of EM Fields

In Figure 11, we display the 2D spatial FFTs of the out-of-plane EM fields (color coded on the right side) as functions of both wave-numbers k_x and k_y in the simulation plane. By dashed contours we plot the fundamental (F) and second harmonic (H) emissions expected at ω_{pe} and $2\,\omega_{pe}$. Only the emissions obtained in case 1 approach these dashed lines, e.g.,

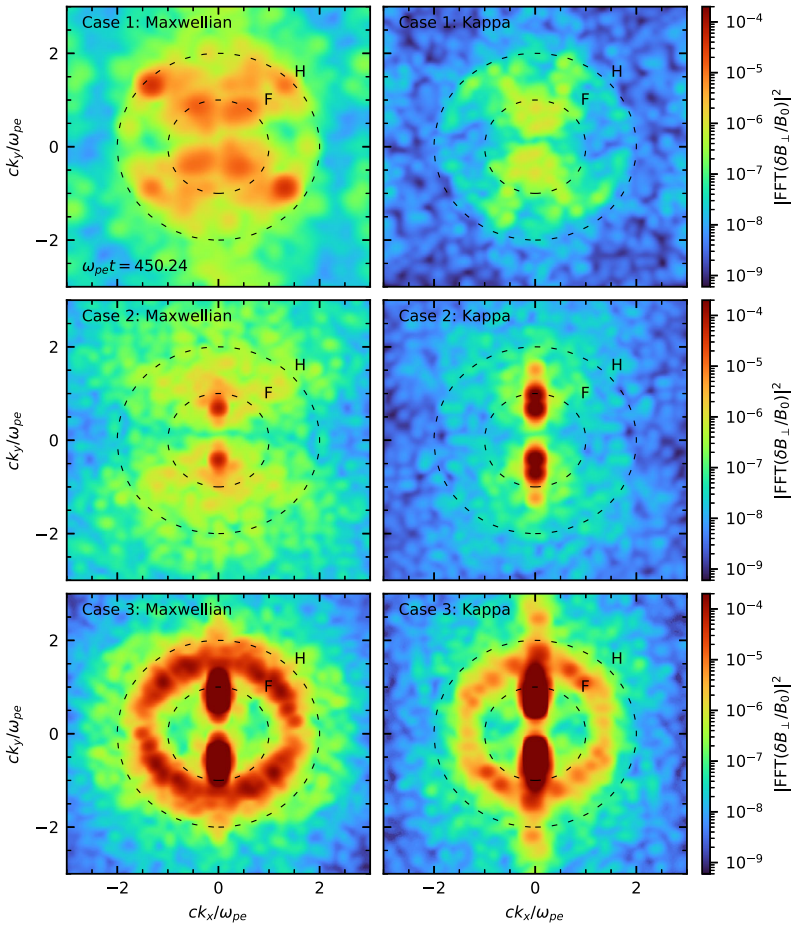

Figure 11 2D spatial FFT, ck_x/ω_{pe} vs. ck_y/ω_{pe}, of the out-of-plane EM emissions generated nonlinearly after the saturation of ES instability, at $\omega_{pe}t \simeq 450$ for all cases, from simulations with Maxwellian (left) and Kappa electrons (right).

for $k_y > 0$, whereas in case 3 the spectra show a significant down-shift in wave numbers and frequencies. These spectra can help to quantify the properties of radio emissions and to understand the nonlinear wave–wave interactions from which they originate.

We chose later snapshots, at $\omega_{pe}t \simeq 450$ after the saturation of the ES instabilities, to differentiate between various fluctuating EM fields resulting from the nonlinear decay of the enhanced ES fluctuations. We can thus distinguish between radio emissions with a more or less isotropic distribution ($k_{x,y} \neq 0$), e.g., in cases 1 and 3, and the highly anisotropic EM waves with perpendicular propagation ($k \simeq k_y$), e.g., in cases 2 and 3. These late spectra appear dominated by the perpendicular emissions with very high intensities, especially for the case where the electrons are (initially) Kappa distributed. Thurgood and Tsiklauri (2015) discussed Weibel-like fluctuations with a major contribution to the energy density of nonlinear EM emissions. In our case, in the presence of the background magnetic field, we can associate these emissions with the ordinary mode (O-mode), which can be excited and powered by the filamentation (Weibel-like) instability of the electron beams.

Acknowledgments The authors acknowledge support from the Ruhr-University Bochum, the Katholieke Universiteit Leuven, and Mansoura University. These results were also obtained in the framework of the projects C14/19/089 (C1 project Internal Funds KU Leuven), G.0D07.19N (FWO-Vlaanderen), WEAVE project – G.0025.23N (FWO-Vlaanderen/DFG-Germany), SIDC Data Exploitation (ESA Prodex-12), Belspo project B2/191/P1/SWiM. R.A.L. acknowledges the support of ANID Chile through FONDECyT grant No. 11201048. Powered@NLHPC: This research was partially supported by the supercomputing infrastructure of the NLHPC (ECM-02).

Author contributions All authors made substantial contributions to the conception and content of the work.

Data Availability All data generated or analyzed during this study are included in this published paper.

Declarations

Competing interests The authors declare no competing interests.

References

Bale, S.D., Reiner, M.J., Bougeret, J.-L., Kaiser, M.L., Krucker, S., Larson, D.E., Lin, R.P.: 1999, The source region of an interplanetary type II radio burst. *Geophysical Research Letters* **26**(11), 1573. DOI.

Baumgärtel, K.: 2014, Ion dynamics in electron beam–plasma interaction: particle-in-cell simulations. *Annales Geophysicae* **32**(8), 1025. DOI. ADS.

Cairns, I.H.: 1989, Electrostatic wave generation above and below the plasma frequency by electron beams. *Physics of Fluids B: Plasma Physics* **1**(1), 204. DOI. ADS.

Cremades, H., Iglesias, F.A., St. Cyr, O.C., Xie, H., Kaiser, M.L., Gopalswamy, N.: 2015, Low-frequency type-II radio detections and coronagraph data employed to describe and forecast the propagation of 71 CMEs/shocks. *Solar Physics* **290**(9), 2455. DOI. ADS.

Crosley, M.K., Osten, R.A., Broderick, J.W., Corbel, S., Eislöffel, J., Grießmeier, J.-M., van Leeuwen, J., Rowlinson, A., Zarka, P., Norman, C.: 2016, The search for signatures of transient mass loss in active stars. *The Astrophysical Journal* **830**(1), 24. DOI.

Fried, B.D.: 1959, Mechanism for instability of transverse plasma waves. *Physics of Fluids* **2**(3), 337. DOI.

Fried, B.D., Conte, S.D.: 1961, *The Plasma Dispersion Function*, Academic Press, New York.

Fuselier, S.A., Gurnett, D.A., Fitzenreiter, R.J.: 1985, The downshift of electron plasma oscillations in the electron foreshock region. *Journal of Geophysical Research* **90**(A5), 3935. DOI. ADS.

Gaelzer, R., Yoon, P.H., Umeda, T., Omura, Y., Matsumoto, H.: 2003, Harmonic Langmuir waves. II. Turbulence spectrum. *Physics of Plasmas* **10**(2), 373. DOI.

Ganse, U., Kilian, P., Vainio, R., Spanier, F.: 2012, Emission of type II radio bursts – single-beam versus two-beam scenario. *Solar Physics* **280**(2), 551. DOI. ADS.

Gary, S.P.: 1985, Electrostatic instabilities in plasmas with two electron components. *Journal of Geophysical Research: Space Physics* **90**(A9), 8213. DOI. ADS.

Gary, S.P.: 1993, *Theory of Space Plasma Microinstabilities*, *Cambridge Atmospheric and Space Science Series*, Cambridge University Press, Cambridge DOI.

Graham, D.B., Cairns, I.H.: 2015, The Langmuir waves associated with the 1 December 2013 type II burst. *Journal of Geophysical Research: Space Physics* **120**(6), 4126. DOI.

Gurnett, D.A.: 1985, *Plasma Waves and Instabilities*, Am. Geophys. Union, Washington, 207. 9781118664179. DOI.

Henri, P., Sgattoni, A., Briand, C., Amiranoff, F., Riconda, C.: 2019, Electromagnetic simulations of solar radio emissions. *Journal of Geophysical Research: Space Physics* **124**(3), 1475. DOI.

Jebaraj, I.C., Kouloumvakos, A., Magdalenic, J., Rouillard, A.P., Mann, G., Krupar, V., Poedts, S.: 2021, Generation of interplanetary type II radio emission. *Astronomy and Astrophysics* **654**, A64. DOI. ADS.

Kasaba, Y., Matsumoto, H., Omura, Y.: 2001, One- and two-dimensional simulations of electron beam instability: generation of electrostatic and electromagnetic $2f_p$ waves. *Journal of Geophysical Research* **106**(A9), 18693. DOI. ADS.

Lacombe, C., Mangeney, A., Harvey, C.C., Scudder, J.D.: 1985, Electron plasma waves upstream of the Earth's bow shock. *Journal of Geophysical Research: Space Physics* **90**(A1), 73. DOI.

Lazar, M., Fichtner, H. (eds.): 2021, *Kappa Distributions; from Observational Evidences via Controversial Predictions to a Consistent Theory of Nonequilibrium Plasmas*, *Astrophysics and Space Science Library* **464**. DOI. ADS.

Lazar, M., Fichtner, H.: 2021b, Kappa distribution function: from empirical to physical concepts. In: Lazar, M., Fichtner, H. (eds.) *Kappa Distributions; from Observational Evidences via Controversial Predictions to a Consistent Theory of Nonequilibrium Plasmas*, *Astrophysics and Space Science Library* **464**, 107. DOI. ADS.

Lazar, M., Fichtner, H., Yoon, P.H.: 2016, On the interpretation and applicability of κ-distributions. *Astronomy and Astrophysics* **589**, A39. DOI.

Lazar, M., Poedts, S., Fichtner, H.: 2015, Destabilizing effects of the suprathermal populations in the solar wind. *Astronomy and Astrophysics* **582**, A124. DOI.

Lazar, M., Schlickeiser, R., Shukla, P.K.: 2008, Cumulative effect of the Weibel-type instabilities in symmetric counterstreaming plasmas with kappa anisotropies. *Physics of Plasmas* **15**(4), 042103. DOI. ADS.

Lazar, M., Schlickeiser, R., Wielebinski, R., Poedts, S.: 2009, Cosmological effects of Weibel-type instabilities. *The Astrophysical Journal* **693**(2), 1133. DOI.

Lazar, M., Pomoell, J., Poedts, S., Dumitrache, C., Popescu, N.A.: 2014, Solar wind electron strahls associated with a high-latitude CME: Ulysses observations. *Solar Physics* **289**(11), 4239. DOI. ADS.

Lazar, M., Pierrard, V., Poedts, S., Fichtner, H.: 2020, Characteristics of solar wind suprathermal halo electrons. *Astronomy and Astrophysics* **642**, A130. DOI.

Lazar, M., Shaaban, S.M., López, R.A., Poedts, S.: 2022a, About the effects of solar wind suprathermal electrons on electrostatic waves. *Astrophysics and Space Science* **367**(10), 104. DOI. ADS.

Lazar, M., López, R.A., Shaaban, S.M., Poedts, S., Yoon, P.H., Fichtner, H.: 2022b, Temperature anisotropy instabilities stimulated by the solar wind suprathermal populations. *Frontiers in Astronomy and Space Sciences* **8**, 249. DOI.

Lazar, M., López, R.A., Moya, P.S., Poedts, S., Shaaban, S.M.: 2023, The aperiodic firehose instability of counter-beaming electrons in space plasmas. *Astronomy and Astrophysics* **670**, A85. DOI.

Lee, S.-Y., Ziebell, L.F., Yoon, P.H., Gaelzer, R., Lee, E.S.: 2019, Particle-in-cell and weak turbulence simulations of plasma emission. *The Astrophysical Journal* **871**(1), 74. DOI.

Lee, S.-Y., Yoon, P.H., Lee, E., Tu, W.: 2022, Simulation of plasma emission in magnetized plasmas. *The Astrophysical Journal* **924**(1), 36. DOI.

Lin, R.P.: 1997, Observations of the 3D distributions of thermal to near-relativistic electrons in the interplanetary medium by the wind spacecraft. In: Trottet, G. (ed.) *Coronal Physics from Radio and Space Observations* **483**, 93. DOI.

Lin, R.P., Potter, D.W., Gurnett, D.A., Scarf, F.L.: 1981, Energetic electrons and plasma waves associated with a solar type III radio burst. *The Astrophysical Journal* **251**, 364. DOI.

Lin, R.P., Levedahl, W.K., Lotko, W., Gurnett, D.A., Scarf, F.L.: 1986, Evidence for nonlinear wave-wave interactions in solar type III radio bursts. *The Astrophysical Journal* **308**, 954. DOI.

Lobzin, V.V., Krasnoselskikh, V.V., Schwartz, S.J., Cairns, I., Lefebvre, B., Décréau, P., Fazakerley, A.: 2005, Generation of downshifted oscillations in the electron foreshock: a loss-cone instability. *Geophysical Research Letters* **32**(18), L18101. DOI. ADS.

López, R.A., Lazar, M., Shaaban, S.M., Poedts, S., Moya, P.S.: 2020, Alternative high-plasma beta regimes of electron heat-flux instabilities in the solar wind. *The Astrophysical Journal Letters* **900**(2), L25. DOI.

López, R.A., Shaaban, S.M., Lazar, M.: 2021, General dispersion properties of magnetized plasmas with drifting bi-Kappa distributions. DIS-K: dispersion solver for kappa plasmas. *Journal of Plasma Physics* **87**(3), 905870310. DOI.

Maksimovic, M., Zouganelis, I., Chaufray, J.-Y., Issautier, K., Scime, E.E., Littleton, J.E., Marsch, E., McComas, D.J., Salem, C., Lin, R.P., Elliott, H.: 2005, Radial evolution of the electron distribution functions in the fast solar wind between 0.3 and 1.5 AU. *Journal of Geophysical Research: Space Physics* **110**, A09104. DOI. ADS.

Manley, J.M., Rowe, H.E.: 1956, Some general properties of nonlinear elements-part I. general energy relations. *Proceedings of the IRE* **44**(7), 904. DOI.

Mann, G., Breitling, F., Vocks, C., et al.: 2018, Tracking of an electron beam through the solar corona with LOFAR. *Astronomy and Astrophysics* **611**, A57. DOI.

Matsumoto, H., Omura, Y. (eds.): 1993, *Computer Space Plasma Physics: Simulation Techniques and Software*, Terra Scientific Publishing Company, Tokyo.

Micera, A., Zhukov, A.N., López, R.A., Innocenti, M.E., Lazar, M., Boella, E., Lapenta, G.: 2020, Particle-in-cell simulation of whistler heat-flux instabilities in the solar wind: heat-flux regulation and electron halo formation. *The Astrophysical Journal Letters* **903**(1), L23. DOI.

Morosan, D.E., Carley, E.P., Hayes, L.A., Murray, S.A., Zucca, P., Fallows, R.A., McCauley, J., Kilpua, E.K.J., Mann, G., Vocks, C., Gallagher, P.T.: 2019, Multiple regions of shock-accelerated particles during a solar coronal mass ejection. *Nature Astronomy* **3**, 452. DOI. ADS.

Nieves-Chinchilla, T., Viñas, A.F.: 2008, Solar wind electron distribution functions inside magnetic clouds. *Journal of Geophysical Research: Space Physics* **113**(A2), A02105. DOI. ADS.

Omura, Y., Matsumoto, H., Miyake, T., Kojima, H.: 1996, Electron beam instabilities as generation mechanism of electrostatic solitary waves in the magnetotail. *Journal of Geophysical Research: Space Physics* **101**(A2), 2685. DOI.

Onsager, T.G., Holzworth, R.H.: 1990, Measurement of the electron beam mode in Earth's foreshock. *Journal of Geophysical Research: Space Physics* **95**(A4), 4175. DOI.

Píša, D., Santolík, O., Hospodarsky, G.B., Kurth, W.S., Gurnett, D.A., Souček, J.: 2016, Spatial distribution of Langmuir waves observed upstream of Saturn's bow shock by Cassini. *Journal of Geophysical Research: Space Physics* **121**(8), 7771. DOI.

Pick, M., Vilmer, N.: 2008, Sixty-five years of solar radioastronomy: flares, coronal mass ejections and Sun Earth connection. *The Astronomy and Astrophysics Review* **16**, 1. DOI.

Pierrard, V., Lazar, M.: 2010, Kappa distributions: theory and applications in space plasmas. *Solar Physics* **267**, 153. DOI.

Pierrard, V., Lemaire, J.: 1996, Lorentzian ion exosphere model. *Journal Geophysical Research: Space Physics* **101**(A4), 7923. DOI.

Pierrard, V., Lazar, M., Poedts, S., Štverák, Š., Maksimovic, M., Trávníček, P.M.: 2016, The electron temperature and anisotropy in the solar wind. Comparison of the core and halo populations. *Solar Physics* **291**(7), 2165. DOI.

Pulupa, M., Bale, S.D.: 2008, Structure on interplanetary shock fronts: type II radio burst source regions. *The Astrophysical Journal* **676**(2), 1330. DOI.

Pulupa, M.P., Bale, S.D., Kasper, J.C.: 2010, Langmuir waves upstream of interplanetary shocks: dependence on shock and plasma parameters. *Journal of Geophysical Research: Space Physics* **115**(A4), A04106. DOI.

Ratcliffe, H., Brady, C.S., Che Rozenan, M.B., Nakariakov, V.M.: 2014, A comparison of weak-turbulence and particle-in-cell simulations of weak electron-beam plasma interaction. *Physics of Plasmas* **21**(12), 122104. DOI.

Reid, H.A.S., Ratcliffe, H.: 2014, A review of solar type III radio bursts. *Research in Astronomy and Astrophysics* **14**(7), 773. DOI.

Rhee, T., Ryu, C.-M., Woo, M., Kaang, H.H., Yi, S., Yoon, P.H.: 2009, Multiple harmonic plasma emission. *The Astrophysical Journal* **694**(1), 618. DOI.

Scherer, K., Husidic, E., Lazar, M., Fichtner, H.: 2022, Revisiting Ulysses electron data with a triple fit of velocity distributions. *Astronomy and Astrophysics* **663**, A67. DOI.

Scudder, J.D.: 1992, Why all stars should possess circumstellar temperature inversions. *The Astrophysical Journal* **398**, 319. DOI.

Shaaban, S.M., Lazar, M., Poedts, S.: 2018b, Clarifying the solar wind heat flux instabilities. *Monthly Notices of the Royal Astronomical Society* **480**(1), 310. DOI.

Shaaban, S.M., Lazar, M., Yoon, P.H., Poedts, S.: 2018a, Beaming electromagnetic (or heat-flux) instabilities from the interplay with the electron temperature anisotropies. *Physics of Plasmas* **25**(8), 082105. DOI.

Shaaban, S.M., Lazar, M., Yoon, P.H., Poedts, S., López, R.A.: 2019, Quasi-linear approach of the whistler heat-flux instability in the solar wind. *Monthly Notices of the Royal Astronomical Society* **486**(4), 4498. DOI.

Soucek, J., Píša, D., Santolík, O.: 2019, Direct measurement of low-energy electron foreshock beams. *Journal of Geophysical Research: Space Physics* **124**(4), 2380. DOI. ADS.

Stverak, S., Travnicek, P., Maksimovic, M., Marsch, E., Fazakerley, A.N., Scime, E.E.: 2008, Electron temperature anisotropy constraints in the solar wind. *Journal of Geophysical Research: Space Physics* **113**(A3), A03103. DOI.

Thejappa, G.: 2022, Evidence for the three wave interactions in the vicinity of an interplanetary shock. *The Astrophysical Journal* **937**(1), 28. DOI.

Thejappa, G., MacDowall, R.J., Bergamo, M.: 2012, In situ detection of strong Langmuir turbulence processes in solar type III radio bursts. *Journal of Geophysical Research: Space Physics* **117**(A8), A08111. DOI.

Thurgood, J.O., Tsiklauri, D.: 2015, Self-consistent particle-in-cell simulations of fundamental and harmonic plasma radio emission mechanisms. *Astronomy and Astrophysics* **584**, A83. DOI.

Vasyliunas, V.M.: 1968, A survey of low-energy electrons in the evening sector of the magnetosphere with OGO 1 and OGO 3. *Journal of Geophysical Research: Space Physics* **73**, 2839. DOI.

Verscharen, D., Chandran, B.D.G., Boella, E., et al.: 2022, Electron-driven instabilities in the solar wind. *Frontiers in Astronomy and Space Sciences* **9**, 951628. DOI.

Villadsen, J., Hallinan, G.: 2019, Ultra-wideband detection of 22 coherent radio bursts on M dwarfs. *The Astrophysical Journal* **871**(2), 214. DOI.

Weibel, E.S.: 1959, Spontaneously growing transverse waves in a plasma due to an anisotropic velocity distribution. *Physical Review Letters* **2**(3), 83. DOI.

Wilson, L.B., Chen, L.-J., Wang, S., Schwartz, S.J., Turner, D.L., Stevens, M.L., Kasper, J.C., Osmane, A., Caprioli, D., Bale, S.D., Pulupa, M.P., Salem, C.S., Goodrich, K.A.: 2019a, Electron energy partition across interplanetary shocks. I. Methodology and data product. *The Astrophysical Journal Supplement Series* **243**(1), 8. DOI.

Wilson, L.B., Chen, L.-J., Wang, S., Schwartz, S.J., Turner, D.L., Stevens, M.L., Kasper, J.C., Osmane, A., Caprioli, D., Bale, S.D., Pulupa, M.P., Salem, C.S., Goodrich, K.A.: 2019b, Electron energy partition across interplanetary shocks. II. Statistics. *The Astrophysical Journal Supplement Series* **245**(2), 24. DOI.

Yi, S., Yoon, P.H., Ryu, C.-M.: 2007, Multiple harmonic plasma emission. *Physics of Plasmas* **14**(1), 013301. DOI.

Yoon, P.H., Gaelzer, R., Umeda, T., Omura, Y., Matsumoto, H.: 2003, Harmonic Langmuir waves. I. Nonlinear dispersion relation. *Physics of Plasmas* **10**(2), 364. DOI.

Ziebell, L.F., Petruzzellis, L.T., Yoon, P.H., Gaelzer, R., Pavan, J.: 2016, Plasma emission by counter-streaming electron beams. *The Astrophysical Journal* **818**(1), 61. DOI.

Authors and Affiliations

M. Lazar[1,2] · R.A. López[1,3] · S. Poedts[1,4] · S.M. Shaaban[5,6]

✉ M. Lazar
marian.lazar@kuleuven.be

1 Centre for Mathematical Plasma Astrophysics, KU Leuven, Celestijnenlaan 200B, 3001, Leuven, Belgium

2 Institute for Theoretical Physics IV, Faculty for Physics and Astronomy, Ruhr-University Bochum, D-44780 Bochum, Germany

3 Departamento de Física, Universidad de Santiago de Chile, Usach, 9170124 Santiago, Chile

4 Institute of Physics, University of Maria Curie-Skłodowska, Pl. M. Curie-Skłodowska 5, 20-031 Lublin, Poland

5 Mathematics, Statistics and Physics Dept., College of Arts and Sciences, Qatar University, Doha, Qatar

6 Theoretical Physics Research Group, Physics Dept., Faculty of Science, Mansoura University, 35516, Mansoura, Egypt